Electrochemical properties of nanofibers α-MoO₃ as cathode materials for Li batteries

A.M. Hashem [a,b], H. Groult [a], A. Mauger [c], K. Zaghib [d,*], C.M. Julien [a]

[a] Université Pierre et Marie Curie, Physicochimie des Electrolytes, Colloïdes et Sciences Analytiques (PECSA), UMR 7195, 4 place Jussieu, 75005 Paris, France
[b] National Research Centre, Inorganic Chemistry Department, Behoes St., Dokki, Cairo, Egypt
[c] Université Pierre et Marie Curie, Institut de Minéralogie et Physique de la Matière Condensée (IMPMC), 4 place Jussieu, 75005 Paris, France
[d] Institut de Recherche d'Hydro-Québec, 1800 Bd Lionel-Boulet, Varennes, Québec, Canada J3X 1S1

HIGHLIGHTS

► Overall, addresses the comparison between bulk and wood-like α-MoO₃ materials.
► Investigation of the local structure of MoO₃ nanofibers synthesized by hydrothermal method.
► Electrochemical properties of α-MoO₃ nanofibers.
► Mechanism of Li insertion and local structure of lithiated phase studied by Raman spectroscopy.

ARTICLE INFO

ABSTRACT

MoO₃ nanofibers have been synthesized by hydrothermal reaction from acidified ammonium hepta-molybdate tetrahydrate precursor. Characterization included X-ray diffraction (XRD), scanning electron microscopy (SEM), SQUID magnetometry and Raman scattering (RS) spectroscopy. Structural analysis shows that MoO₃ nanofibers 50–80 nm in diameter and a several micrometers in length are grown in the orthorhombic system (*Pbnm* S.G.). The composition MoO$_{2.9975}$ was determined by Rietveld refinement and magnetic susceptibility measurements. The electrochemical performance of Li//MoO₃ cells with nanofibers deliver a better discharge capacity after 40 cycles than MoO₃ bulk. Raman spectroscopy studies revealed the structural modulation upon Li intercalation in MoO₃ nanofibers. The possible mechanism of intercalation is discussed.

1. Introduction

Molybdenum oxides (MoO$_x$) exhibit interesting structural, chemical, electrical, and optical properties, which are dependent on the growth conditions and the fabrication technique. They show promise in many applications, ranging from electronics to energy storage and micromechanics [1]. With diverse morphological structures, MoO$_x$ materials have a wide range of potential applications. When nano-structured, they have applications in the fields of display devices, sensors [2], electrochromics [3], lubricants [4], field-emission-devices [5], organic solar cells [6], battery electrodes

[7] and pseudocapacitors [8]. Moreover, molybdenum oxides are important compounds in selective oxidation catalysis [9,10].

One of the most interesting properties of nano-structured MoO$_x$ is their intercalation ability, which is possible only if the binding between the layers or tunnels of the host material is weak. Nano-structured MoO$_x$ are used in electrochemical systems as either positive or negative electrode materials; they have been prepared by various synthetic methods: α-MoO₃ micro-rods by vapor transportation method [11], nanobelts by hydrothermal reaction [12], nanobelts encapsulated with poly(ethylene glycol) [13], MoO₃ nanoparticles by hot-wire chemical vapor deposition (HWCVD) [14,15]. While different studies have examined the bulk and nanobelt structural chemistry and electrochemical behavior related to the Li intercalation of MoO₃, little is known about the comparison with MoO₃ nanofibers [16–18].

In this paper, we report the structural and electrochemical properties of nanostructured molybdenum trioxide materials that are one-dimensional microstructures of the orthorhombic α-MoO_3 phase. Nanofibers, *i.e.* wood-like materials, are considered. The structure and morphology are characterized by X-ray diffraction (XRD), scanning electron microscopy (SEM), SQUID magnetometry and Raman scattering (RS) spectroscopy. The electrochemical features of MoO_x used as cathodes in lithium batteries are presented and compared with those of bulk α-MoO_3.

2. Experimental

Bulk MoO_3 single crystals were prepared by the well-known dehydration of the molybdic acid followed by heat treatment at 750 °C for 10 h [19]. This method provides large platelets that are individual (010)-oriented MoO_3 transparent crystals. One-dimensional microstructures, wood-like MoO_3 were synthesized via acidification to pH = 3.5 of a solution of ammonium hepta-molybdate tetrahydrate $(NH_4)_6Mo_7O_{24} \bullet 4H_2O)$ (from Fisher Scientific Inc. $\geq$ 99.0%), using diluted glacial acetic acid. This intermediate compound was then placed in a Teflon-lined stainless steel autoclave heated at 170−185 °C for 6 days. After filtration and washing with a solution of deionized water and ethanol, the final fibrous sample was dried and sintered at 500 °C for 4 h.

XRD data were obtained using a Philips X'Pert diffractometer equipped with a Cu anticathode (CuK$_\alpha$ radiation λ = 1.5406 Å). XRD patterns were collected under Bragg−Brentano geometry at 2θ with step 0.02° in the range 10−80°. The SEM images were collected using a Hitachi S-4700 microscope in the ultra-high-resolution mode. Magnetization measurements have been performed using an SQUID magnetometer (Quantum Design MPMS XL5). The applied field was H = 5000 Oe and the data were obtained in the temperature range from 4 to 300 K. Raman spectra were recorded on a Jobin-Yvon U1000 double monochromator using the 632.8 nm line from a He−Ne laser. Standard photon-counting techniques were used for detection. In a typical spectral acquisition, six RS spectra each recorded with a resolution of 2 cm^{-1} were averaged. Care was taken against sample photo-decomposition using low excitation power of 100 W cm^{-2}.

The electrochemical evaluations of a-MoO_3 nanofibers were accomplished by assembling coin cells with the configuration Li/ 1 mol L^{-1} LiPF$_6$ solution of EC-DEC (1:1)/MoO_3. The positive electrode was made by dispersing 85 wt.% active materials of α-MoO_3 nanofibers, 10 wt.% polyvinylidene fluoride (PVdF) binder and 5 wt.% acetylene black conductive agent to form homogeneous slurry, which was uniformly pasted on aluminum foil. A cell was constituted by a pellet cathode pressed at 0.5×10^5 Pa with an area of 0.8 cm^2 cathode, a glass-fiber separator (Whatman GF/C), and a lithium-metal foil anode. This assembly was sandwiched between nickel foils as current collectors. Electrochemical titration measurements were carried out using a Mac-Pile system at current densities in the range 0.1−0.2 mA cm^{-2}.

3. Results and discussion

3.1. Structural studies

Fig. 1a shows the XRD diffraction patterns of MoO_3 nanofibers and α-MoO_3 crystalline (bulk) for comparison. The main features of the XRD patterns can be indexed in orthorhombic system (*Pbnm* S.G.). The XRD diagram of α-MoO_3 single crystal displays essentially the sharp (0k0) Bragg lines that identify the elongated platelets with the (010) axis perpendicular to the basal plane and the (001) axis along the longest edge. Fig. 2 displays the layered arrangement causes van der Waals interactions between parallel layers formed
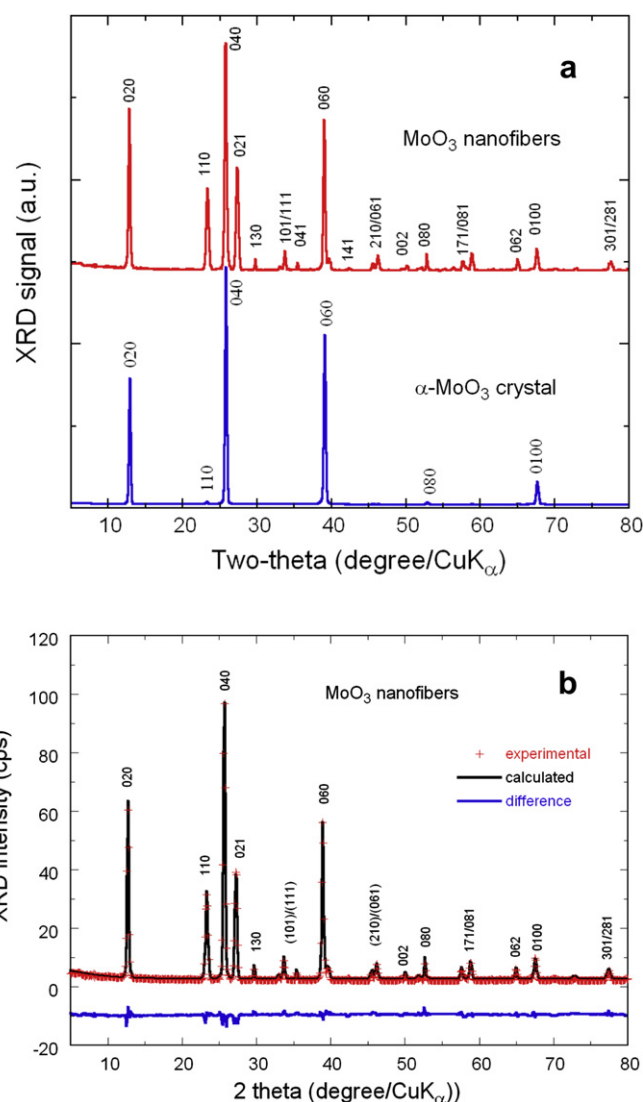

Fig. 1. (a) XRD patterns of the α-MoO_3 nanofibers compared with the α-MoO_3 bulk synthesized from dehydration of the molybdic acid. (b) Rietveld refinement of the XRD data of α-MoO_3 nanofibers.

by MoO_6 octahedra that share edges in the (001) direction and are connected by corners in the (100) direction. As shown in this scheme, two types of empty sites are available for hosting foreign ions like lithium. The (0k0) intense Bragg lines suggest that this
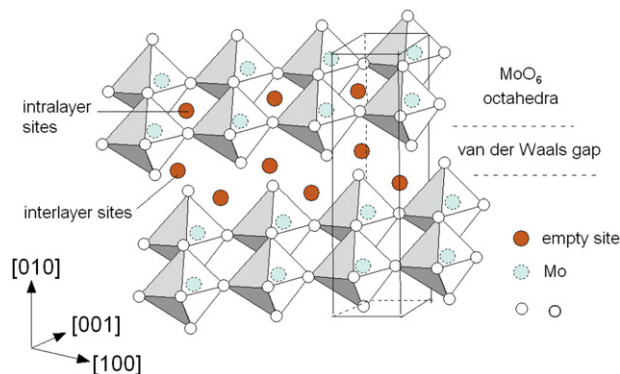

Fig. 2. Scheme of the MoO_3 structure showing the available empty sites for Li insertion into the orthorhombic structure.

compound is a layered structure packed in the direction of the *b*-axis. Lattice parameters are found to be $a = 3.962(5)$ Å, $b = 13.858(8)$ Å, $c = 3.697(3)$ Å, and $V = 202.98$ Å^3. The XRD diagram of MoO$_3$ nanofibers displays sharp peaks indicating a well crystallized nanostructure. Similarly to the α-MoO$_3$ crystal, the Bragg lines can be indexed in the orthorhombic lattice (*Pbnm* S.G.) without any impurity phase. Fig. 1b shows the refinements of the XRD data of the nanofibers obtained with the Rietveld parameters $R_{Bragg} = 2.8\%$, $R_p = 5.33\%$ $R_{wp} = 9.98$ and $\chi^2 = 1.245$. The lattice constants of the nanofiber structure are $a = 3.952(2)$ Å, $b = 13.853(8)$ Å and $c = 3.701(1)$ Å, $V = 202.61$ Å^3. The Rietveld refinement was achieved form the formula MoO$_{3-\delta}$. The occupancy parameter of the oxygen anions was refined and constrained to be equal to that of Mo^{6+} ions. The result $\delta = 0.002 \pm 0.0005$ shows that the deviation from stoichiometry is very small. The intense (0*k*0) reflections depict an oriented anisotropic growth of the MoO$_{3-\delta}$ nanofibers similarly to nanobelts and nanorods [20,21].

The morphology of MoO$_3$ nanofibers has been investigated by scanning electron microscopy (SEM) as a function of the temperature of the hydrothermal process (Fig. 3a–b). The morphology of the product obtained from the intermediate compound (see section 2) placed in the autoclave heated at 170 °C (image 3a) shows that the fiber-like morphology of most MoO$_3$ nanofibers was not well-retained at this low temperature, while nanofibers synthesized in the autoclave heated at 185 °C for 6 days display the well-developed wood-like MoO$_3$ (image 3b). The dimensions of the fibers are about 50–80 nm in diameter and several micrometers in length. These values compare well with the coherent lengths $L_{(100)} = 44$ nm and $L_{(001)} = 2.65$ μm calculated from XRD data using the Scherrer formula. High-resolution transmission microscopy (TEM) image of an individual nanofiber (Fig. 3c) provides further insight into the structure of this material. It is displayed that the
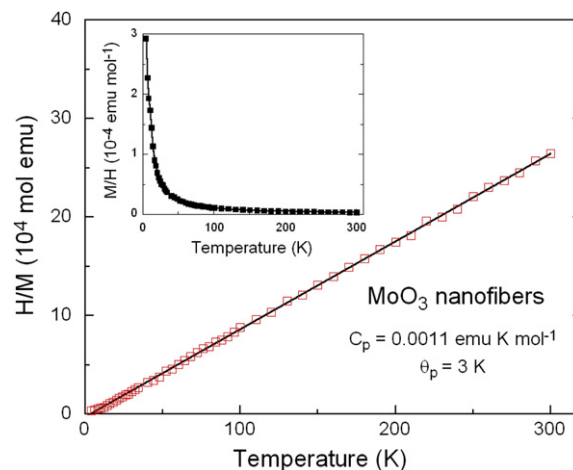

Fig. 4. The temperature dependence of the reciprocal magnetic susceptibility of MoO$_3$ nanofibers. Measurements were carried out with an applied magnetic field $H = 5000$ Oe.

growth axis of the single nanofiber occurs along the <001 > direction of the orthorhombic α-MoO$_3$. Lattice fringe with neighboring spacing (the arrows shown in diagram) of the nanofiber is 0.69(3) nm, about a half of the lattice constant *b* (1.3858 nm) of the orthorhombic structure.

Fig. 4 shows the temperature dependence of the reciprocal magnetic susceptibility of MoO$_3$ nanofibers. Measurements were carried out with an applied magnetic field $H = 5000$ Oe. The insert displays the "zero-field cooling" (ZFC) magnetic susceptibility, *i.e.* data recorded on sample cooled at low temperature without
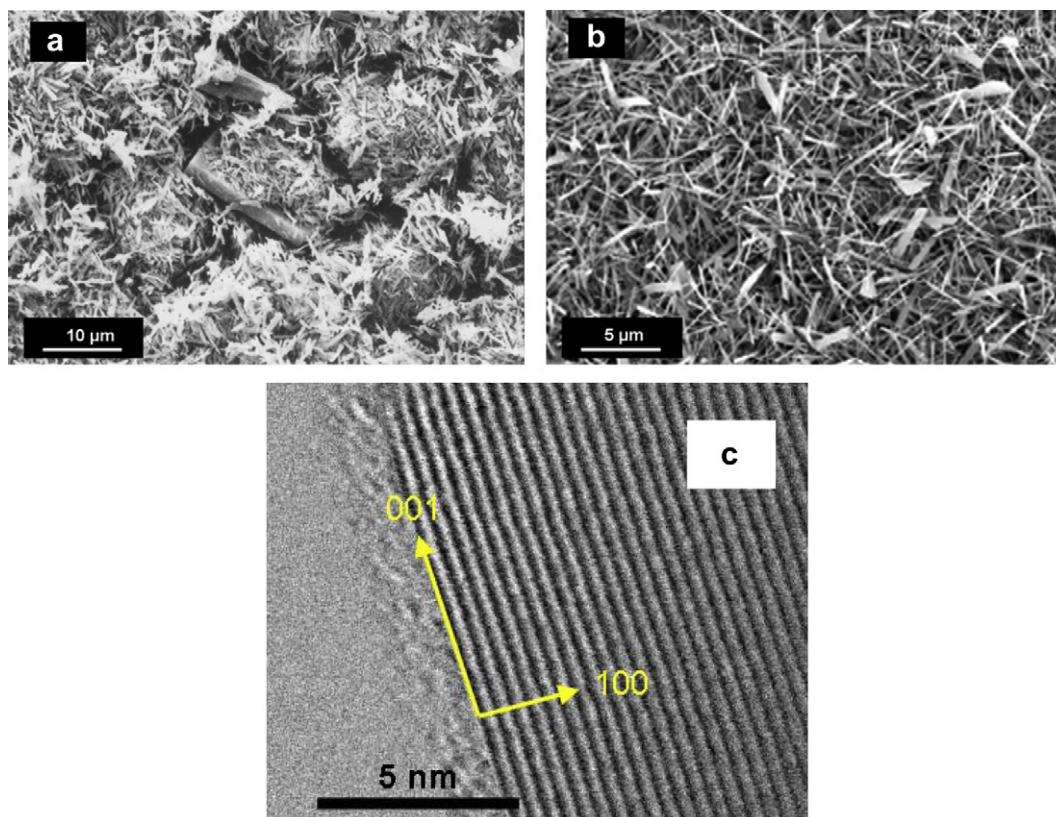

Fig. 3. SEM images of (a) The intermediate compound was placed in the autoclave heated at 170 °C and (b) The nanofibers synthesized in the autoclave heated at 185 °C for 6 days.

applying magnetic field. Obviously, these temperature dependent magnetization measurements corroborate the structural analysis as follows. The data reveal only a small paramagnetic response, which satisfies the Curie–Weiss law

$$\chi_m = \frac{C_p}{T + \theta_p}, \tag{1}$$

where C_p is the Curie constant and θ_p the Weiss constant. Taking into account that the electronic properties of MoO_3 involved non-magnetic ($S = 0$) Mo ions in the oxidation state 6 + without electrons occupying the 4d shell (4d^0), the weak magnetic paramagnetic response shown in Fig. 4 is due to a small concentration of Mo^{5+} ions ($S = 1/2$) in the nanostructured materials. The parameters obtained by least-square fitting (Eq. (1)) are $C_p = 0.0011$ emu K mol^1 and $\theta_p = 3$ K. The effective Bohr magneton number is $p_{eff} = 0.095$. Considering the theoretical effective momentum number for Mo^{5+} ions ($p_{th} = 1.73$), we obtained a concentration $y = 0.003$ of magnetic Mo^{5+} ions; thus the chemical formula of the synthesized nanofilters is $MoO_{2.9985}$, close to the idealized stoichiometry. This composition is in good agreement with the value $\delta = 0.002 + 0.0005$ determined from XRD analysis. The negligible value of θ_p is consistent with the very small value of y, since the distance between the magnetic ions is so large that they cannot interact.

The local structure of α-MoO_3 microfibers was investigated by Raman spectroscopy. Fig. 5 displays the typical RS spectrum of MoO_3 microfibers compared with that of bulk α-MoO_3. Note that the spectra are normalized to the band at 817 cm^{-1} for better comparison. The spectral fingerprints of the α-phase are clearly seen in these Raman spectra, which can be analyzed using the orthorhombic D_{2h}^{16} symmetry. The assignment of the different modes and lattice vibrations can be made according to [22]. It is reported in Table 1. The RS spectrum of α-MoO_3 is dominated by the internal modes involving stretching and bending modes of Mo–O bonds in MoO_6 distorted octahedra that invariably occur in the 1000–600 and 400-200 cm^{-1} spectral regions, respectively. The multiplicity corresponds to the various Mo–O lengths varying from 0.167 to 0.233 nm for the α-MoO_3 structure. The highest Raman band at 994 cm^{-1} is due to the vibration of the shortest Mo=O bonds, the so-called molybdyl mode, whereas the next highest stretching frequency at 817 cm^{-1} is assigned to the intermediate bridging Mo–O–Mo bond. The external modes (lattice modes) are

observed in the opposite side of the spectrum, below 200 cm^{-1}. The RS spectrum of nanofibers displays enhancement in the intensity of several peaks, i.e. the stretching vibration of terminal Mo=O at 994 cm^{-1} (A_g mode), the O–Mo–O scissor at 377 cm^{-1} (B_{1g} mode) and the translational rigid MoO_4 chain mode (B_{3g} mode). These results show that the vibrational modes polarized in the c-direction are sensitive to the morphology of the sample. We also observe a frequency shift for the Mo–O–Mo bending from 478 to 468 cm^{-1} (A_g mode).

3.2. Electrochemical studies

Fig. 6 represents the first discharge–charge curves for Li//MoO_3 cells using 1 mol L^{-1} $LiPF_6$ in EC-DEC (1:1) as electrolytes. Positive electrodes were (a) α-MoO_3 crystal and (b) MoO_3 nanofibers. Electrochemical tests were carried out at C/5 rate in the potential range 1.5–3.5 V vs. Li^+/Li. The first and second discharge curves displaying modification of the insertion reaction are shown in Fig. 6c. Quantification of the intercalation mechanism was deduced from the incremental capacity analysis, $-dQ/dV$ vs. voltage plots that are obtained by numerical differentiation of data in Fig. 6, which gives rise to curves similar to cyclic voltammograms [19]. Results are shown in Fig. 7. The first discharge profile of the Li//α-MoO_3 cell is characterized by an abrupt decrease of the potential followed by two plateaus with the first capacity range 0–50 mA h g^{-1} at ca. 2.81 V and 80-240 mA h g^{-1} at ca. 2.29 V. These plateaus occur at lower potential ~2.78 and 2.17 V in the range $0.08 \leq x \leq 0.20$ and $0.9 \leq x \leq 1.5$, respectively, for MoO_3 nanofibers. Nanofibers deliver a capacity 265 mAh g^{-1} for the first discharge in the potential range 3.5–1.5 V, and the Li uptake is 1.5 Li/Mo. Thus, the electrochemical features of nanofibers are characteristic of a two-phase domain similar to that of bulk α-MoO_3. However, we notice that, as expected, the discharge curve exhibits larger cell polarization for high C-rate, i.e. about 0.6 V at 2C.

Structural evolution of this domain corresponds to a solid solution involving $Li_{0.08}MoO_3$ and $Li_{0.2}MoO_3$ (called α'-MoO_3). The reduced monophase/biphase boundary (Fig. 6) is attributed to the nanosize effect on the electrochemical activity of nanofibers. Upon decreasing the diameter of the particles, experiments show that the plateau is shrinking, which has been interpreted as the sign that the miscibility gap decrease with L [23]. The size effects should be important only at significantly smaller sizes, so that the solution should still be unstable for wood-like particles under surface energy aspects. The first charge is characterized by only one plateau at ca. 2.40 V, which is reversible along the successive cycles (Fig. 6c).
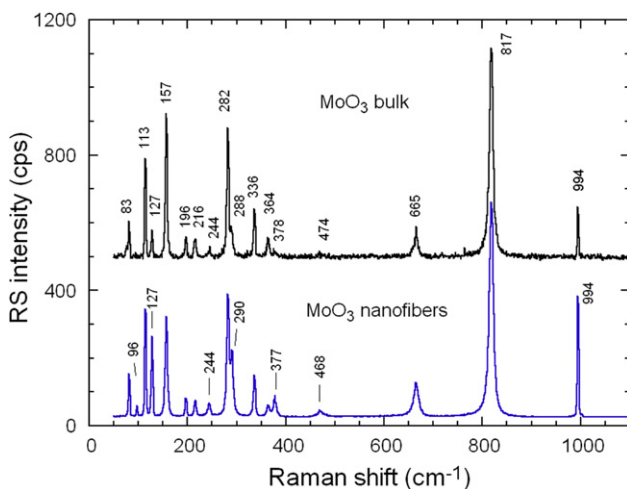

Fig. 5. Raman spectra of α-MoO_3 crystal and nanofibers. Data were collected using the 632.8 nm line of He–Ne laser. The dotted bands in the spectrum of nanofibers are those altered.

Table 1
Experimental Raman modes of single crystalline MoO_3 and band assignment according to [22].

| Raman shift (cm^{-1})	Species	Assignment
994	A_g	ν_{as} O=Mo stretch
817	A_g	ν_s O=Mo=O stretch
665	B_{2g}/B_{3g}	ν Mo–O–Mo stretch
474–468	A_g	ν Mo–O–Mo stretch and bend
377–378	B_{1g}	δ O=Mo=O scissors
364	A_g	δ O=Mo=O scissors
336	A_g/B_{1g}	δ Mo–O–Mo bend
288–290	B_{3g}	δ O=Mo=O waging
282	B_{2g}	δ O=Mo=O waging
244	B_{3g}	τ O=Mo=O twist
216	A_g	Rotational rigid MoO_4-chain mode, R_c
196	B_{2g}	τ O=Mo=O twist
157	A_g/B_{1g}	Translational rigid MoO_4-chain mode, T_b
127	B_{3g}	Translational rigid MoO_4-chain mode, T_c
113	B_{2g}	Translational rigid MoO_4-chain mode, T_c
96	B_{1g}	Translational rigid MoO_4-chain mode, T_a
83	A_g	Translational rigid MoO_4-chain mode, T_a
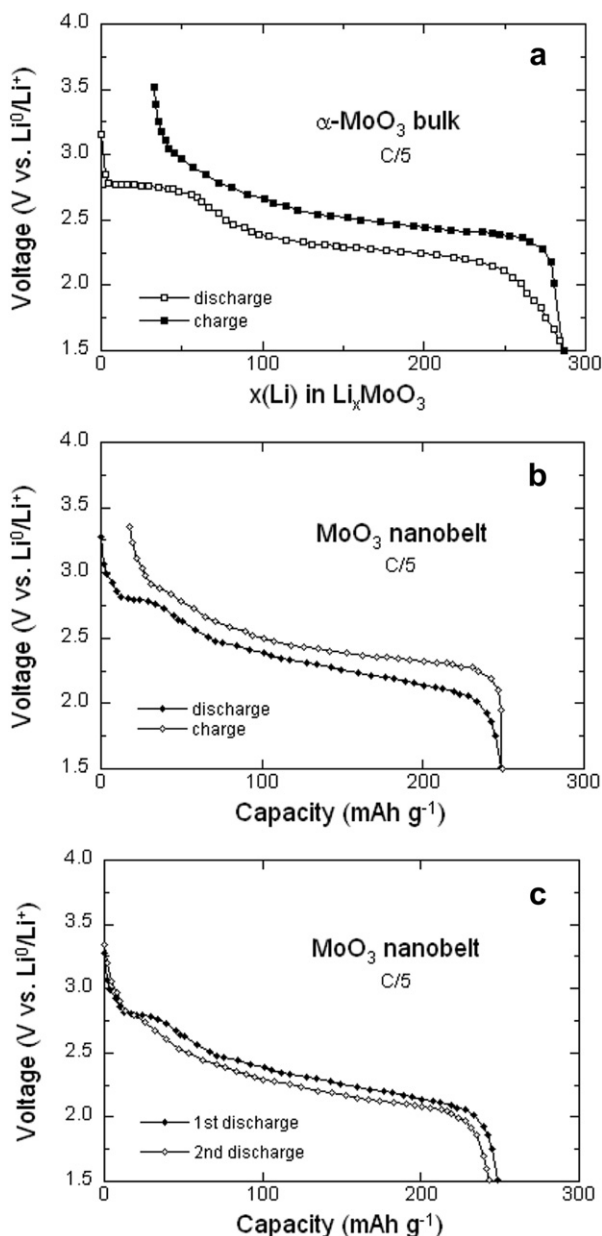
Fig. 6. First discharge–charge curves for Li//MoO$_3$ cells using 1 mol L^{-1} LiPF$_6$ in EC-DEC (1:1) as electrolytes. Positives electrodes were (a) α-MoO$_3$ crystal, and (b) nanofibers. Electrochemical tests were carried out at C/5 rate in the potential range 1.5–3.5 V vs. Li/Li$^+$. (c) The first and second discharge profile for α-MoO$_3$ nanofibers.

Fig. 8 shows the variation of the discharge capacity vs. C-rate for α-MoO$_3$ bulk and MoO$_3$ nanofibers. The rate performance is one of the most important properties for cathode materials. The MoO$_3$ nanofibers synthesized by the hydrothermal process show a stabilized charge-discharge performance as an insertion type electrode material at high rate conditions. It is obvious from Fig. 8 that MoO$_3$ nanofibers show a good reversibility of Li$^+$ at higher current densities compared with bulk MoO$_3$. As a general trend, high rate performance is achieved by nanostructure engineering and surface modification of wood-like MoO$_3$, owing to the control of the morphology and size of the active materials. The cycle performance of the MoO$_3$ nanofilters battery is shown in Fig. 9. The reversible capacity of MoO$_3$ nanofibers is compared to α-MoO3 crystal as a function of the cycle number. Electrochemical tests were carried out at C/5 rate in the potential range 1.5–3.5 V vs. Li/Li$^+$. After
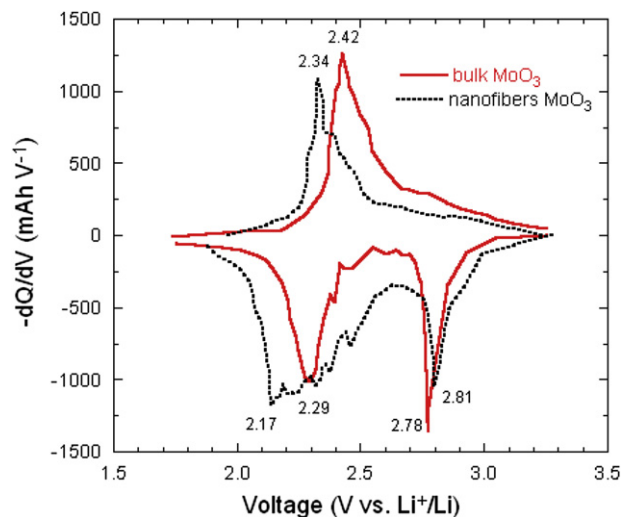

Fig. 7. The incremental capacity analysis, −dQ/dV vs. voltage, calculated from electrochemical data of Fig. 5.

40 cycles, the capacity loss is smaller with the MoO$_3$ nanofibers, which indicates their satisfactory electrochemical properties. This is attributed to the special one-dimensional morphology of MoO$_3$ nanofibers with the orthorhombic structure that contains a large number of tetrahedral and octahedral cavities allowing for easy reversible intercalation and deintercalation reaction. The difference of the electrochemical properties between MoO$_3$ nanofibers and MoO$_3$ bulk powder is clearly depicted in Figs. 7–9, in which we observed (1) a small shift of the redox potential toward lower voltage, ΔV, of 80−100 mV for the MoO$_3$ nanofibers as shown in the incremental capacity curves, (b) a better discharge capacity delivered for C-rate higher than 1C due the nanosize effect of the fibers and (c) a much better electrochemical performance upon cycle number for the nanofibers. The capacity loss is only 0.17% per cycle for MoO$_3$ nanofibers against 0.64% for MoO$_3$ bulk which indicates that the MoO$_3$ nanofiber battery exhibits satisfactory electrochemical properties. This is attributed to a distinctive layered structure (orthorhombic) and a special one-dimensional morphology of the MoO$_3$ nanofibers. Notice that the α-MoO$_3$ nanofibers have a large aspect ratio and special surface area.
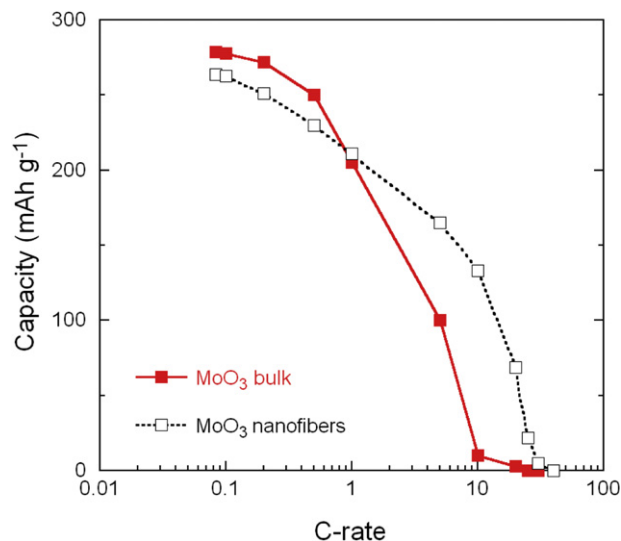

Fig. 8. The variation of the discharge capacity vs. C-rate for α-MoO$_3$ bulk and MoO$_3$ nanofibers. Electrochemical data were collected in the range 1.5–3.5 V vs. Li$^+$/Li.
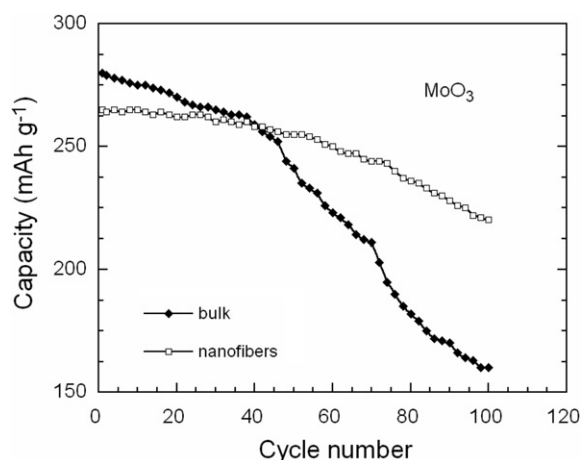
Fig. 9. Reversible capacity of α-MoO3 crystal and MoO3 nanofibers as a function of the cycle number. Electrochemical tests were carried out at C/5 rate in the potential range 1.5–3.5 V vs. Li/Li$^+$.

Fig. 11. Raman spectra of MoO$_3$ nanofibers as a function of the amount of Li$^+$-ions inserted. Arrows point out the new Raman bands of the LiMoO$_3$ phase.

The disappearance of the irreversible peak (at ca. 2.8 V vs. Li/Li$^+$) in the incremental capacity curves is related to a structural modulation that occurs upon insertion/extraction of Li$^+$ ions between the MoO$_6$ octahedral inter-layers and intra-layers, respectively, and it is responsible for a capacity loss of ca. 40 mAh g^{-1}. Indeed, the first plateau at 2.78 V for nanofibers disappeared in the second and following discharge processes. This suggests that part of the Li$^+$ ions, first introduced during the reduction reaction (discharge), later remain in the lattice. Such an effect has also been observed in V$_2$O$_5$ [24] The mechanism of Li-ions intercalation into the α-MoO$_3$ has been described as the formation of three phases separated by bi-phase domains that are responsible for voltage plateaus in the first discharge curve [7,25,26]. It is believed that the Li$_{0.25}$MoO$_3$ phase formed at 2.7 V vs. Li/Li$^+$ is at the origin of the irreversible capacity at the end of the first charge. Thus, for subsequent cycles of discharge-charge, the cathode material shuttles from Li$_{0.25}$MoO$_3$ to Li$_{1.5}$MoO$_3$ without the appearance of the first plateau. Based on these results, an idealized scheme of the Li intercalation process into the MoO$_3$ framework is shown in Fig. 10.
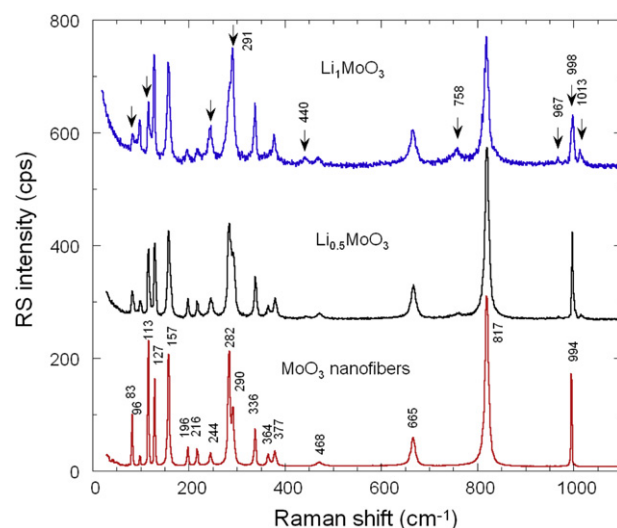
The evolution of the local structure of cathode materials during the first discharge has been studied by Raman spectroscopy. The electrode was washed with DMC solution to remove LiPF$_6$ salt and left in a glove box for 12 h to reach equilibrium. Fig. 11 shows the Raman spectra of MoO$_3$ nanofibers as a function of the concentration of Li$^+$-ions inserted in the range $0 \le x \le 1$. At the first discharge, the Raman spectrum of MoO$_3$ nanofibers shows significant changes. As a general trend, we notice that all the main spectral features observed in MoO$_3$ are present in the spectrum of Li$_x$MoO$_3$ and the broadening of the bands indicate that the Li$_x$MoO$_3$ phase is less ordered than the α-MoO$_3$ lattice. On comparing the Raman features of Li$_x$MoO$_3$ and MoO$_3$, the following considerations can be established: (i) the intensity of the translational modes at low frequency, i.e. 83 and 113 cm^{-1}, is progressively quenched, (ii) some bands are enhanced, i.e. the δ(O$_2$–Mo–O$_2$) scissoring B_{3g} and B_{1g} modes at 244 and 377 cm^{-1}, respectively, while some others vanish, i.e. the intense δ(O$_1$–Mo–O$_1$) wagging B_{2g} mode at
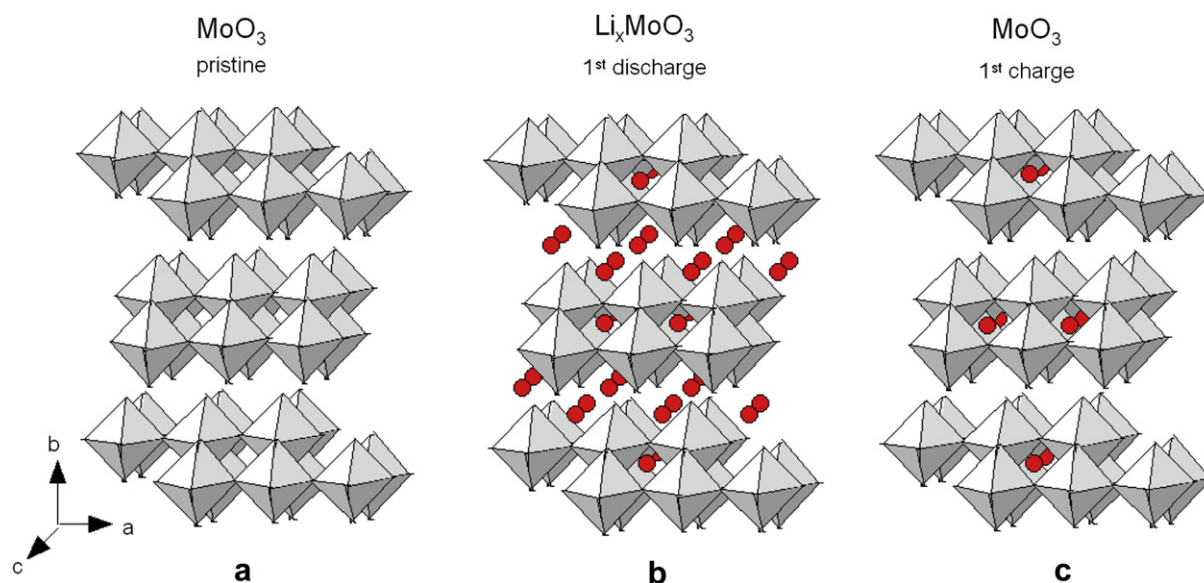

Fig. 10. Idealized scheme of the intercalation process in MoO$_3$ framework. At the end of the discharge, the chemical composition is Li$_{1.5}$MoO$_3$, while at the end of the charge, it is Li$_{0.25}$MoO$_3$.

282 cm^{-1} and the $\delta(O_2{-}Mo{-}O_2)$ scissoring A_g mode at 364 cm^{-1}, (iii) the single line, corresponding to the Mo=O stretching mode (molybdyl mode) along the c-axis broaden and shifted up to 998 cm^{-1} with respect to 994 cm^{-1}, typically observed for the α-phase, and (iv)new spectral features are detected in the spectrum of Li$_x$MoO$_3$ (bands at 440, 758, 967 and 1013 cm^{-1}). At least two factors can account for the distinction between the spectra of these materials. First, the non-equivalent character of the transition metals in the lattice of Li$_x$MoO$_3$, meaning three kinds of molybdenum oxidation states from Mo^{6+} to Mo^{4+}, which implies the modification in the local environment of MoO$_6$ octahedra. Second, the Li atom oscillations may couple with some modes of the MoO$_3$ lattice. These results are consistent with the reported data in the literature, which describe that the lithium insertion process consists in rather moderate local distortions allowing the accommodation of 1.5 Li/mol of oxide without breaking of the orthorhombic symmetry [7].

4. Conclusion

In this work, MoO$_3$ nanofibers were synthesized by hydrothermal reaction from acidified ammonium heptamolybdate tetrahydrate precursor. Structural analysis shows that MoO$_3$ nanofibers 50–80 nm in diameter and a several micrometers in length are grown in the orthorhombic system (*Pbnm* S.G.) of the α-MoO$_3$ phase. The stoichiometric deviation, *i.e.* oxygen defects δ, was determined by Rietveld refinement and magnetic susceptibility measurements with $\delta = 0.002 + 0.0005$. The electrochemical tests of Li//MoO$_3$ cells show that nanofibers deliver a better discharge capacity after 40 cycles than MoO$_3$ bulk, and have better performance at high current density. Raman spectroscopy studies have revealed the structural modulation upon Li intercalation in MoO$_3$ nanofibers with the Li atom oscillations that couple with

some modes of the MoO$_3$ lattice. The possible mechanism of intercalation has been discussed based on the disappearance of the first plateau at ca. 2.7 V.

References

[1] D.A. Scherson, A. Palencsar, ECS Interface 15 (2006) 17.
[2] A.K. Prasad, D.J. Kubinski, P.I. Gouma, Sens. Actuators B 93 (2003) 25.
[3] C.G. Granquist, Appl. Phys. 57 (1993) 3.
[4] J. Wang, K.C. Rose, C.M. Lieber, J. Phys. Chem. B 103 (1999) 8405.
[5] J. Zhou, N.-S. Xu, S.-Z. Deng, J. Chen, J.-C. She, Z.-L. Wang, Adv. Mater. 15 (2003) 1835.
[6] L. Cattin, M. Morsli, F. Dahou, S. Yapi Abe, A. Khelil, J.C. Bernede, Thin Solid Films 518 (2010) 4560.
[7] T. Tsumura, M. Inagaki, Solid State Ionics 104 (1997) 183.
[8] T. Brezesinski, J. Wang, S.H. Tolbert, B. Dunn, Nat. Mater. 9 (2010) 146.
[9] Y. Tong, J.H. Lundsford, J. Am. Chem. Soc. 113 (1991) 4741.
[10] R.K. Grasselli, J.D. Burrington, Adv. Catal. 30 (1981) 133.
[11] W. Li, F. Cheng, Z. Tao, J. Chen, J. Phys. Chem. B 110 (2006) 119.
[12] L. Mai, B. Hu, W. Chen, Y. Qi, C. Lao, R. Yang, Y. Dai, Z.L. Wang, Adv. Mater. 19 (2007) 3712.
[13] V.S. Reddy, E.H. Walker Jr., C. Wen, S. Mho, J. Power Sources 183 (2008) 330.
[14] A.C. Dillon, A.H. Mahan, R. Deshpande, P.A. Parilla, K.M. Jones, S. Lee, Thin Solid Films 516 (2008) 794.
[15] S.H. Lee, Y.H. Kim, R. Deshpande, P.A. Parilla, E. Whitney, D.T. Gillaspie, K.M. Jones, A.H. Muhan, S. Zhang, A.C. Dillon, Adv. Mater. 20 (2008) 3627.
[16] K. Dewangan, N.N. Sinha, P.K. Sharma, A.C. Pandey, N. Munichandraiah, N.S. Gajbhiye, Cryst. Eng. Comm. 13 (2010) 927.
[17] P.I. Gouma, Rev. Adv. Mater. Sci. 5 (2003) 147.
[18] Z. Peng, L. Jing, W. Lin, Z. Baohua, Y. Liuxiao, F. Huiqing, Synth. React. Inorg. 38 (2008) 318.
[19] C. Julien, G.A. Nazri, Solid State Ionics 68 (1994) 111.
[20] S. Wang, Y. Zhang, X. Ma, W. Wang, X. Li, Z. Zhang, Y. Qian, Solid State Commun. 136 (2005) 283.
[21] X.W. Lou, H.C. Zeng, Chem. Mater. 14 (2002) 4781.
[22] M.A. Py, Ph.E. Schmid, J.T. Vallin, Il Nuovo Cimento 38B (1977) 271.
[23] C.M. Julien, A. Mauger, K. Zaghib, J. Mater. Chem. 21 (2011) 9955.
[24] F. Leroux, B.E. Loene, L.F. Nazar, J. Electrochem. Soc. 143 (1996) L181.
[25] Y. Iriyama, T. Abe, M. Inaba, Z. Ogumi, Solid State Ionics 135 (2000) 95.
[26] A.M. Hashem, M.H. Askar, M. Winter, J.H. Albering, J.O. Besenhard, Ionics 13 (2007) 3.